Laser-generated toroidal helium plasmas

Kooij, V.L.

2

Generation and optical analysis of transient toroidal helium plasmas

We experimentally studied laser-generated, atmospheric pressure, transient toroidal helium plasmas. For the entire evolution of these toroidal plasmas, we present tomographically reconstructed, poloidal radiant intensity profiles, that clearly visualise the formative fluid flow. A new splitting of the toroidal plasma is observed during the final phase of its evolution. We present a model based on elementary thermodynamic principles that establishes a characteristic time scale at which structure is expected to develop, supported by measurements of the density of helium atoms in the centre of the toroidal plasma. We report on the repeated creation of plasma observed during the creation of a laser-induced breakdown plasma, which possibly contributes to the formation of the two-lobe structure visible in its plasma kernel. We briefly touch upon a possible application of the laser-generated toroidal helium plasmas in the study of self-organising knotted magnetic structures.

2.1 *Introduction*

The work presented in this chapter is in preparation for publication in the *Journal of Plasma Physics*.

In contemporary nuclear fusion research, magnetic confinement fusion is generally regarded as the most prominent approach. Understanding the stability of these magnetically confined plasmas is therefore of fundamental importance, and the topology of the confining fields proves to play a pivotal role.

The connection between stability and topology has been established in 1969, when Moffatt found that helicity, the quantity identified by Woltjer to be conserved in a plasma with infinite conductivity,[1] is in fact a measure of the degree of linkage and knottedness of magnetic field lines.[2]

[1] Woltjer 1958.

[2] Moffatt 1969.

Recently, the connection between stability and topology has been confirmed by magnetohydrodynamics simulations, demonstrating that an initially helical magnetic field reconfigures itself into a configuration

of foliated toroidal surfaces.[3] These self-organising knotted magnetic structures are intrinsically stable, and their configuration is essentially different from that of a tokamak, in that their hydrostatic pressure is minimal on the central circle of the foliated tori. The magnetic energy density of these knotted plasma structures is highly localised.

As already mentioned in the introduction of this dissertation, toroidal plasma structures have been observed in a vast range of experimental settings, including nanosecond discharges, laser ignition of flammable mixtures, high-power electric arcs, high-speed micro jets, and laser-induced breakdown plasmas.[4] In the course of our earlier exploratory investigations using laser-induced breakdown plasmas, we observed toroidal plasma structures that are far more symmetrical than those reported in the aforementioned studies.

An example of the development of these toroidal plasmas, generated in quiescent atmospheric pressure helium gas at room temperature, is presented in figure 2.1. Their self-confined toroidal nature and atmospheric pressure ambient conditions provide an interesting setting for investigating the numerically predicted and intrinsically stable self-organising knotted magnetic structures in plasma.[5]

In this chapter we investigate the prime features responsible for the development of these laser-generated toroidal helium plasmas. We present tomographically reconstructed, poloidal radiant intensity profiles, for the entire evolution of a toroidal plasma, with which the formative fluid flow is clearly visualised. A new splitting of the toroidal

[3] Smiet, Candelaresi et al. 2015.

[4] Stepanyan et al. 2019; Dumitrache et al. 2017; Bradley et al. 2004; Bak, Im et al. 2014; Seward 2014; Gharib et al. 2017; Nassif et al. 2000; Harilal et al. 2015; Bak, Wermer et al. 2015.

[5] Smiet, Candelaresi et al. 2015.

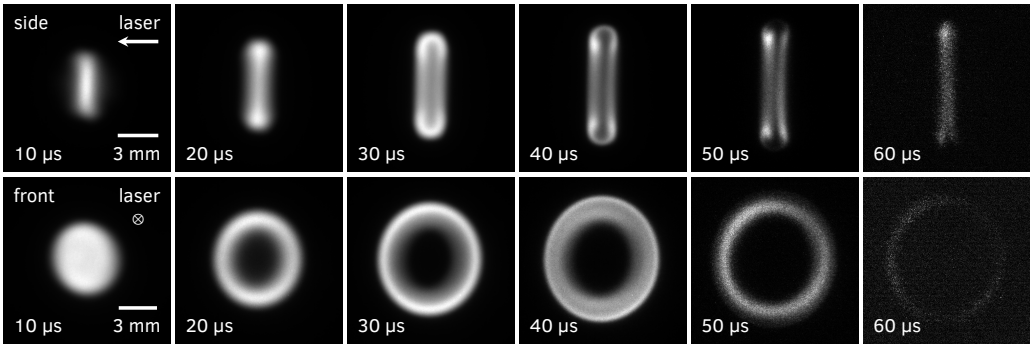

Figure 2.1: Development of a toroidal plasma due to a single laser-induced breakdown plasma, generated in quiescent atmospheric pressure helium gas at room temperature. Side view images (top row) and front view images (bottom row) have been captured at increasing times (left to right) after the breakdown laser pulse. All images have been averaged over 50 exposures and captured through a 10 nm bandpass filter with a centre wavelength of 590 nm. The front view images show slightly oval plasma structures due to a necessary skewed viewing direction. All images have been individually normalised to their maximum intensity to respect the large dynamic range in intensity of the entire development. See section 2.3 for further experimental details.

plasma is observed during the final phase of its evolution.

The characteristic time scale observed in the development of the toroidal plasma will be explained by an intuitive model based on elementary thermodynamic principles. The time scale thus obtained is supported by the evolution of the density of helium atoms in the centre of the toroidal plasma, measured with the use of a second laser-induced breakdown plasma.

An essential element in the development of the toroidal plasmas is the symmetric repletion of a low density cavity, generated in the wake of the shock formed by a laser-induced breakdown plasma. In support, we present flow experiments where the symmetrical experimental setting is deliberately broken, and analyse the resulting fluid flow using tomographically reconstructed, poloidal radiant intensity profiles.

We briefly discuss the repeated creation of plasma observed during the creation of a laser-induced breakdown plasma. These repeating dynamics possibly contributes to the formation of the two-lobe structure visible in the plasma kernel.

2.2 *Experimental details*

A simplified schematic[6] of the pulsed high power optical set-up used in the presented experiments is shown in figure 2.2. Two Q-switched Nd:YAG lasers (Quanta-Ray GCR-3 and Continuum NY61-10) provide

[6] For a more lively impression of the experimental set-up we refer to photo 1 on page 103.

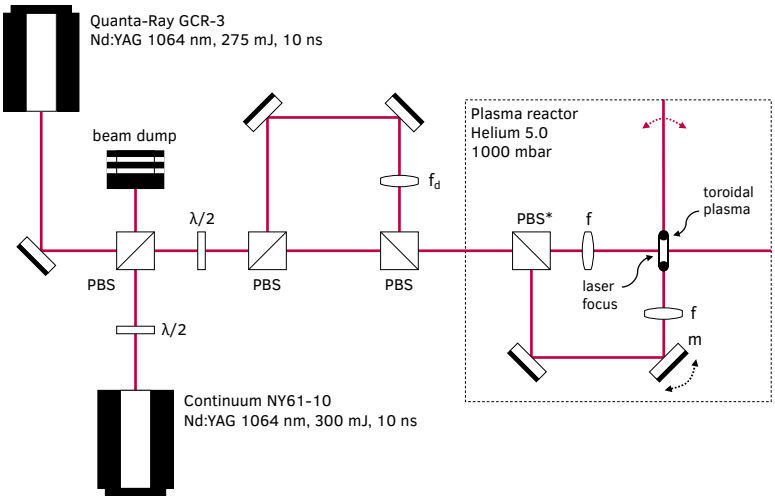

Figure 2.2: Simplified schematic of the pulsed high power optical set-up. PBS: polarising beam splitter, PBS*: removable polarising beam splitter, $\lambda/2$: half-wave plate, f: focusing lens, f_d: lens to slightly displace the focus inside the plasma reactor, m: rotating mirror. For a more lively impression of the experimental set-up we refer to photo 1 on page 103.

high power laser pulses with a wavelength of 1064 nm, a temporal pulse length of approximately 10 ns, and a beam width of 8 mm. The pulse energy is adjustable between 0 and 275 mJ (or 300 mJ for the Continuum NY61-10) which is accomplished by routing the laser pulse through two attenuators (not shown) each consisting of a half-wave plate and a polarising beam splitter. The laser pulse energy is measured using a laser power meter (Ophir Nova II and PE50BF-C) just before entering the plasma reactor.

Particular experiments demand successive laser pulses to be generated with intervals as short as a few tens of nanoseconds. This can be accomplished by using both lasers simultaneously and combining their laser beam paths. This is achieved by rotating the polarisation of the laser pulses from one laser by 90° using a half-wave plate and combining both pulses using a polarising beam splitter. The combined beam path carries horizontally polarised (p-polarised) laser pulses from the Quanta-Ray laser and vertically polarised (s-polarised) laser pulses from the Continuum laser.

Before the laser pulses enter the plasma reactor, the combined beam path is split and recombined again, to provide a means of modifying the vertically polarised laser pulses, just before they enter the plasma reactor (see figure 2.2). In section 2.5, this possibility is used to slightly displace the focus of the vertically polarised laser pulses inside the plasma reactor, with respect to the focus of the horizontally polarised laser pulses, using a diverging plano-concave lens f_d with a focal length of 2 m. With this adjustment, it is possible to simultaneously create two closely spaced plasmas and study the effect they have on each other.

Inside the plasma reactor, the laser pulses are focused into quiescent atmospheric pressure 5.0 grade helium gas using a 1" plano-convex lens with a focal length of 50 mm (Thorlabs LA1131-YAG) to produce a laser-induced breakdown plasma.

For experiments visualising shocks using a second laser-induced breakdown plasma,[7] a removable polarising beam splitter inside the plasma reactor is used to split-off the vertically polarised laser pulses, which are subsequently focused at a 90° angle with respect to the original beam path (see figure 2.2). This angle can be adjusted slightly using a piezoelectric inertia actuator, making it possible to use one laser to scan through a plasma created earlier using the other laser.

[7] These experiments will be presented in chapter 3.

The Q-switch and flash lamp trigger signals for both lasers are generated by a digital delay generator (Stanford Research Systems DG645) and an in-house designed FPGA (field-programmable gate array) based reconfigurable pulse generator. The flash lamps operate

at a repetition rate of 10 Hz while the Q-switches operate at a reduced repetition rate of 2.5 Hz.

The radiant intensity[8] of the plasma decreases orders of magnitude during its evolution from a laser-induced breakdown plasma to the final toroidal plasma. When studying the toroidal plasma, emission from the initial and very bright breakdown plasma can cause artefacts in the recorded images. The reduced repetition rate minimises unnecessary emission leaking through the MCP (micro-channel plate[9]) of the ICCD (intensified CCD) camera (Princeton Instruments PI-MAX 512) while attaining the maximum possible image capture rate.

[8] Radiant intensity is defined as the energy emitted per unit time per unit solid angle.

[9] A micro-channel plate is closely related to an electron multiplier. In ICCD cameras it acts as image intensifier and nanosecond time scale shutter.

The ICCD camera receives a trigger from the digital delay generator before the Q-switch is triggered, so that it is possible to image the onset of a laser-induced breakdown plasma.

The digital delay generator also generates a trigger signal for a 1 GHz bandwidth oscilloscope (LeCroy LT584L) used for precise timing analysis, and for recording the temporal profile of the laser pulse and plasma emission using a 150 ps rise time Si photo detector (Thorlabs DET025AFC). The timing resolution of the integral set-up for plasma creation and observation is approximately 4 ns.

The imaging set-up (not shown) consists of two achromatic 4f lens configurations[10] (Thorlabs AC508-300-A and AC508-400-A) capable of simultaneously imaging the side and front view of the toroidal plasma by combining both views through a 50/50 non-polarising beam splitter. The front view is necessary skewed by approximately 26° to avert blocking of the high power laser beam by the imaging optics.

[10] A 4f lens configuration consists of two identical lenses sharing one focal plane (also called the Fourier plane) and provides unit magnification.

The images recorded by the ICCD camera are single shot. During an experiment, plasma is repeatedly created, and every recorded image is captured from a distinct plasma. Due to small fluctuations visible in the single shot images, and to increase the signal to noise ratio, most images presented in this work have been averaged over 50 repetitions.

All images used for quantitative analysis are corrected for flat field, background emission, dark frame, and bias frame. The background correction is performed using the edge columns of the recorded image as a reference, to simultaneously correct for both stray light and diffuse reflections from within the imaging system.

The necessity to perform a flat field correction is nicely illustrated in figure 2.3, where we can see that our flat field image exhibits variations as large as 15%. The honeycomb structure that is visible throughout the image is not unique to our camera, and has been reported previously[11] in the literature.

[11] Williams et al. 2007.

To illustrate the effect of the flat field correction on quantitative

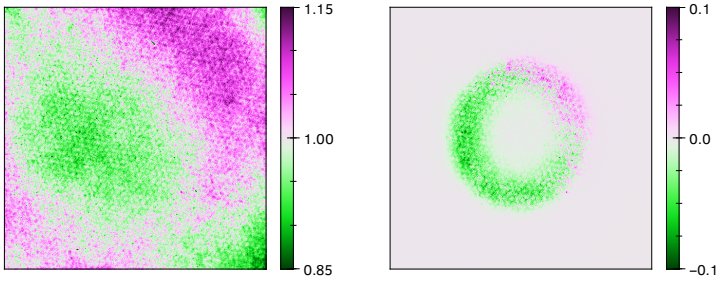

Figure 2.3: (left) Flat field image of our ICCD camera shown in false colour. Note the honeycomb structure that is visible throughout the image. (right) For a typical image of a toroidal plasma, this image shows the difference between the original and flat field corrected image, normalised to the maximum intensity of the original image.

measurements, figure 2.3 shows, for a typical image of a toroidal plasma, the difference between the original and flat field corrected image, normalised to the maximum intensity of the original image. It is clear that variations of up to 10% can be observed.

Imaging the extensive range of radiant intensities of the plasma during its evolution from a laser-induced breakdown plasma to the final toroidal plasma, is accomplished by attenuating the plasma emission using neutral density filters, rather than changing the gain or exposure time of the ICCD camera. This averts possible non-linear behaviour of the ICCD camera contaminating the quantitative measurements.

Density gradients in the helium gas can been visualised[12] using a high-speed Schlieren[13] imaging system, consisting of a low-power 4 mW collimated 632.8 nm helium-neon laser beam (Uniphase 1121P), and a knife edge positioned at the shared focal plane of the 4f lens system used for imaging the side view of the toroidal plasma. A laser line filter (Thorlabs FL632.8-10) has been used to block most plasma emission. The remaining emission that is still visible through the laser line filter is corrected by subtracting images that have been captured while the helium-neon laser was switched off.

[12] These experiments will be presented in chapter 3.

[13] See for a treatise on Schlieren imaging Settles 2001 and references therein.

2.3 *Toroidal plasma development*

The observed self-organising toroidal plasmas emerge solely due to a single laser-induced breakdown plasma, created in quiescent atmospheric pressure helium gas at room temperature. These toroidal structures are plasma afterglows[14] despite the fact that they exhibit intricate structure. This section presents an overview of the evolution leading to these plasma structures. A more detailed description of the prime features will be presented in the following sections.

[14] A plasma afterglow is the radiation emitted from a cooling plasma when the source of ionisation is removed.

In figures 2.4–2.6 the evolution of a single laser-induced breakdown plasma for a laser pulse energy of 250 mJ is presented.[15] These plasmas have been created in quiescent 5.0 grade helium gas at a pressure of 1002 mbar, using a 1" plano-convex lens with a focal length of 50 mm. The images have been recorded using an ICCD camera viewing the plasma orthogonal to the laser propagation direction (side view) and from a slight angle with respect to the laser propagation direction (front view) as explained in section 2.2. Due to the necessary skewed viewing direction, the front view images show slightly oval plasma structures.

All images have been recorded using a fixed gate width of 250 ns and a fixed gain of 255, to avert possible non-linear behaviour of the ICCD camera contaminating the quantitative measurements. Because during its evolution the radiant intensity of the plasma decreases orders of magnitude (see figures 2.7 and 2.9) neutral density filters have been used to attenuate the plasma emission to avert overexposure of the ICCD camera. Overlapping series of images have been recorded, which later have been glued together to obtain a single series of images spanning the complete evolution of the plasma. This is illustrated in figure 2.7, where different series for a given laser pulse energy are alternately represented by line segments and markers. Because the least intense sequences have been recorded without a neutral density filter, series of different laser pulse energies can be compared with each other. Moreover, all images presented in this work have been individually normalised to

[15] Similar evolution is observed for pulse energies of 50, 100, and 200 mJ. Although this work primarily reports on plasmas created with a pulse energy of 250 mJ, this section also presents measurements of the spectral radiant intensity and linear dimensions for plasmas created with a pulse energy of 50, 100, and 200 mJ, and reports on the similar morphology of toroidal plasmas generated with different pulse energies.

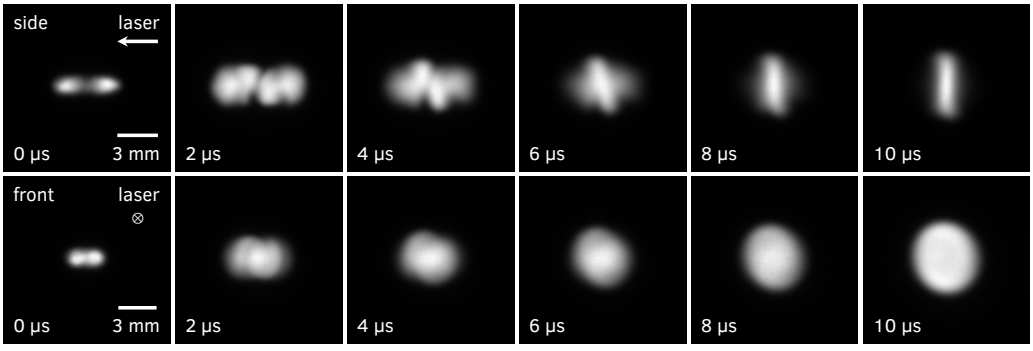

Figure 2.4: First part (0–10 µs) of the development of a toroidal plasma due to a single laser-induced breakdown plasma created in quiescent atmospheric pressure helium gas at room temperature. Side view images (top row) and front view images (bottom row) have been captured at increasing times (left to right) after the breakdown laser pulse. All images have been averaged over 50 exposures and captured through a 10 nm bandpass filter with a centre wavelength of 590 nm. The front view images show slightly oval plasma structures due to a necessary skewed viewing direction. All images have been individually normalised to their maximum intensity to respect the large dynamic range in intensity of the entire development. Laser pulse energy: 250 mJ, focal length focussing lens: 50 mm, gas pressure: 1002 mbar, ICCD camera gate width: 250 ns.

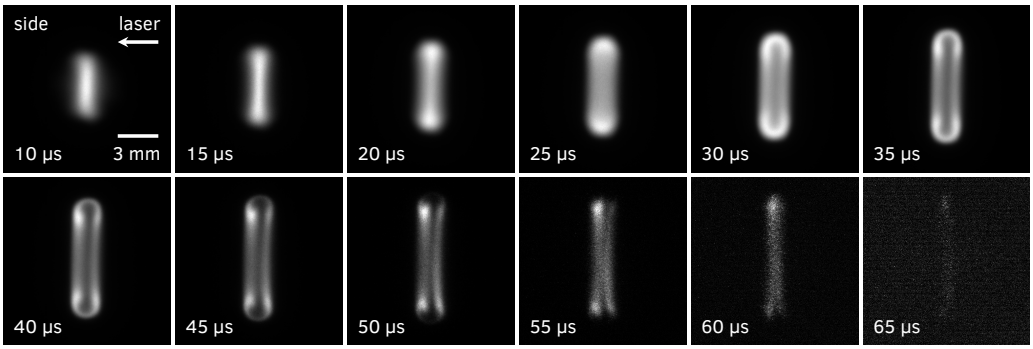

Figure 2.5: Development and subsequent dissolvement of a toroidal plasma due to a single laser-induced breakdown plasma. Side view images have been captured at increasing times (left to right, top to bottom) after the breakdown laser pulse. Note that all images have been individually normalised to their maximum intensity to respect the large dynamic range in intensity of the entire development. The images are a continuation of the development presented in figure 2.4 and have been captured using identical experimental settings as those presented there.

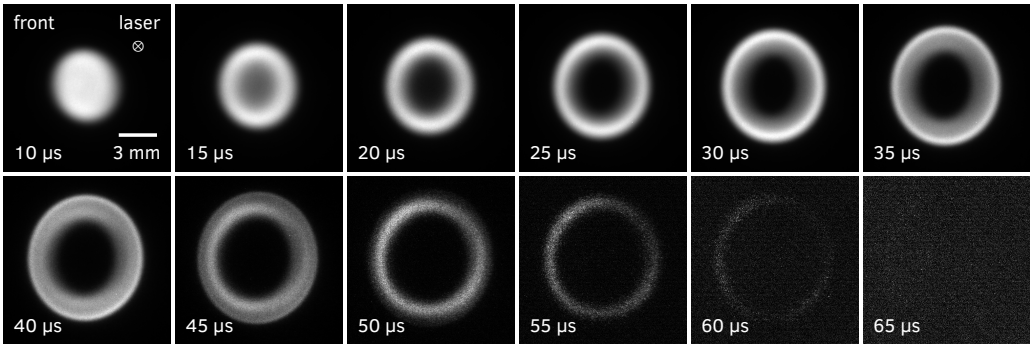

Figure 2.6: Development and subsequent dissolvement of a toroidal plasma due to a single laser-induced breakdown plasma. Front view images have been captured at increasing times (left to right, top to bottom) after the breakdown laser pulse. The images show slightly oval plasma structures due to a necessary skewed viewing direction. Note that all images have been individually normalised to their maximum intensity to respect the large dynamic range in intensity of the entire development. The images are a continuation of the development presented in figure 2.4 and have been captured using identical experimental settings as those presented there.

their maximum intensity to respect the large dynamic range in intensity of the entire development.

The self-organising toroidal plasmas are alike most laboratory plasmas[16] in the sense that they are optically thin[17] and exhibit a line spectrum.[18] Preliminary high-speed spectra recorded using a prism spectrograph coupled to the imaging system of the ICCD camera have shown that most emission originates from neutral atomic helium. In order to facilitate quantitative analysis all images therefore have been captured through a 10 nm bandpass filter with a centre wavelength of 590 nm (Thorlabs FB590-10). This bandpass filter encloses the atomic helium emission lines at 587.6 nm originating from the $1s3d\,^3D$–$1s2p\,^3P$ multiplet transitions.[19] Moreover, to block out-of-band emission a 750 nm short-pass filter (Thorlabs FESH0750) has been used.

It has been noted that all images recorded by the ICCD camera are captured from independent laser-induced breakdown events. The gradual development of the images presented in figures 2.4–2.6 shows

[16] Cooper 1966, pp. 37, 41; Hutchinson 2002, pp. 221–222, 252.

[17] Rybicki et al. 1979, pp. 12–14; Cooper 1966, pp. 41, 90.

[18] Hutchinson 2002, p. 252; Smerlak 2011; Rybicki et al. 1979, p. 17; Schregel et al. 2016; Carbone et al. 2016.

[19] Kramida et al. 2019.

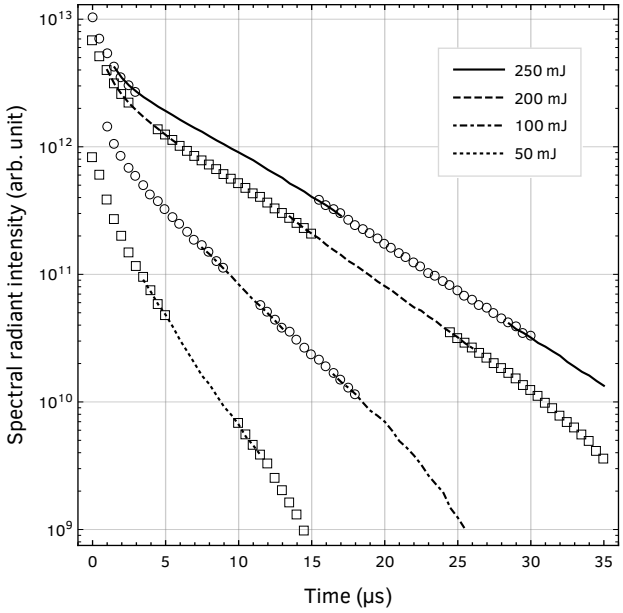

Figure 2.7: Spectral radiant intensity of a laser-induced breakdown plasma created with a pulse energy of 50, 100, 200, and 250 mJ. Overlapping series of images have been recorded, that later have been glued together to obtain a single series of images spanning the complete evolution of the plasma. This graph shows the overlapping series of recordings for a given laser pulse energy, alternately represented by line segments and markers. Note the different time span compared to figure 2.9. This graph is based on the same recordings as those used for figures 2.4–2.6.

that the plasma evolution is very reproducible. Due to small fluctuations visible in the single shot images, and to increase the signal to noise ratio, most notably during the faint afterglow, all images have been averaged over 50 repetitions.

The evolution visible in figures 2.4–2.6 clearly shows the emergence of a toroidal plasma structure from 10 µs onward. Previous laser-induced breakdown studies have reported similar plasma structures,[20] most notably in nitrogen and air. Likewise, recent studies on laser ignition of flammable alkane-air mixtures reported the emergence of toroidal flame kernels.[21]

An almost perfect plasma torus[22] has been formed around 20 µs, which is seen to evolve into an eroded toroid prior to splitting into two halves. This is a new observation and a strong indication that, although the emerged plasma structure is of toroidal nature, it does not exhibit vorticity like the well-known vortex rings[23] or the structures reported in previous studies.[24]

A probable explanation is the symmetry of the breakdown plasma. In figure 2.4 one can see that our laser-induced breakdown plasma at 0 µs exhibits a two-lobe structure which is highly symmetrical with respect to the focal plane. Numerical studies on the fluid dynamical effects of laser energy deposition show[25] that the generation of vorticity found in these systems stems from the asymmetrical tear-drop shape of the breakdown plasma. This suggests that our highly symmetrical breakdown plasma inhibits the generation of vorticity in our toroidal plasma. In section 2.5 a three-dimensional tomographic reconstruction of the plasma will be presented that visualises the symmetrical fluid flow responsible for the emergence of the toroidal structure.

It has been noted that the two-lobe structure of our breakdown plasma does not concord with the cited studies on laser-induced breakdown plasmas. However, they have been reported in recent studies on the onset and dynamics of plasma kernels.[26,27]

Another marked difference between the presented evolution and the cited laser-induced breakdown studies is the characteristic time scale. In our experiment, after 20 µs, an almost perfect plasma torus has been formed, whereas in the cited studies this takes much longer. For example, in Harilal[28] where toroidal structures of similar size in air are studied, this occurs after 50 µs.

An intuitive explanation can be found in the density dependence of the speed of sound in gasses. Because the speed of sound in a gas and the mean speed of its constituents are of the same order of magnitude[29] it is tenable that they dictate how fast density variations equilibrate. For

[20] Nassif et al. 2000; Harilal et al. 2015; Bak, Wermer et al. 2015.

[21] Dumitrache et al. 2017; Bradley et al. 2004; Bak, Im et al. 2014.

[22] At this point it is well to distinguish between a toroid, a surface or solid formed by rotating a closed curve about a line which lies in the same plane but does not intersect it, and a torus, in which the closed curve is a circle.

[23] Akhmetov 2009.

[24] Dumitrache et al. 2017; Nassif et al. 2000; Harilal et al. 2015; Bradley et al. 2004.

[25] Ghosh et al. 2008; Morsy et al. 2002.

[26] Nishihara et al. 2018; Alberti, Munafò, Pantano et al. 2019a.

[27] In section 2.7 plasma kernel dynamics and the two-lobe structure will be addressed in more detail.

[28] Harilal et al. 2015.

[29] Jeans 1940, p. 57.

an ideal gas, the speed of sound is given by[30]

$$c = \sqrt{\gamma \frac{p}{\rho}}$$

where p is the pressure, ρ the mass density, and γ the (constant) ratio of specific heats c_p/c_v. Substitution of tabulated values[31] at standard temperature and pressure[32] reveals that the speed of sound in helium is 2.9 times higher than in air, which is in agreement with our observations. In section 2.5 we will present an intuitive model and derive the observed time scale from elementary thermodynamic principles.

The evolution presented in figures 2.4–2.6 reveals the emergence of features in common with earlier reported laser-induced breakdown studies.[33] These can be summarised as follows.

0 µs — A laser-induced breakdown plasma has been created due to the avalanche ionisation of the helium gas. Multi-photon ionisation provides the initial seed electrons necessary to ignite the avalanche[34]. Subsequent inverse bremsstrahlung absorption heats[35] the plasma, creating a high pressure and high temperature plasma kernel whose rapid expansion leads to the formation of a shock.[36]

1 µs — The plasma kernel continues to expand, while the shock detaches from the kernel and propagates into the quiescent ambient gas, creating a low density cavity in its wake. The shock is not visible in the presented images. See section 3.2 for high-speed Schlieren images visualising the shock up to 4 µs.

2–8 µs — The plasma is squeezed in longitudinal direction (see linear dimensions shown in figure 2.8) due to gas flowing back to the plasma kernel along the symmetry axis. While the plasma is compressed in longitudinal direction it continues to expand in the transverse direction.

10 µs — A plasma pillbox has been formed due to the longitudinal compression and the evolution enters a more quiescent phase.

20 µs — An almost perfect plasma torus has emerged. The flow returning along the symmetry axis squeezed a hole into the plasma pillbox. The plasma torus is approximately 6.5 mm in diameter and 2 mm thick (see figure 2.8) for a laser pulse energy of 250 mJ.

30–40 µs — Due to our highly symmetrical breakdown plasma, the squeezing flow approaches the plasma from both sides equally. These flows will collide in the centre of the torus and expand into a plane orthogonal to the symmetry axis, pushing the plasma outward.[37] The plasma torus evolves into a deformed and eroded toroidal plasma.

50 µs — The flow deforming and eroding the toroidal plasma continues and dissects the toroidal plasma into two halves.

[30] Landau et al. 1987, p. 318.

[31] Haynes 2014.

[32] Standard temperature and pressure is defined as 273.15 K and 10^5 Pa.

[33] Nassif et al. 2000; Harilal et al. 2015; Bak, Wermer et al. 2015.

[34] Raizer 1991, p. 155.

[35] Miziolek et al. 2006, p. 171.

[36] Y. Chen et al. 2000; Harilal et al. 2015; Ghosh et al. 2008.

[37] See section 2.5 for a three-dimensional tomographic reconstruction of the plasma visualising these flows.

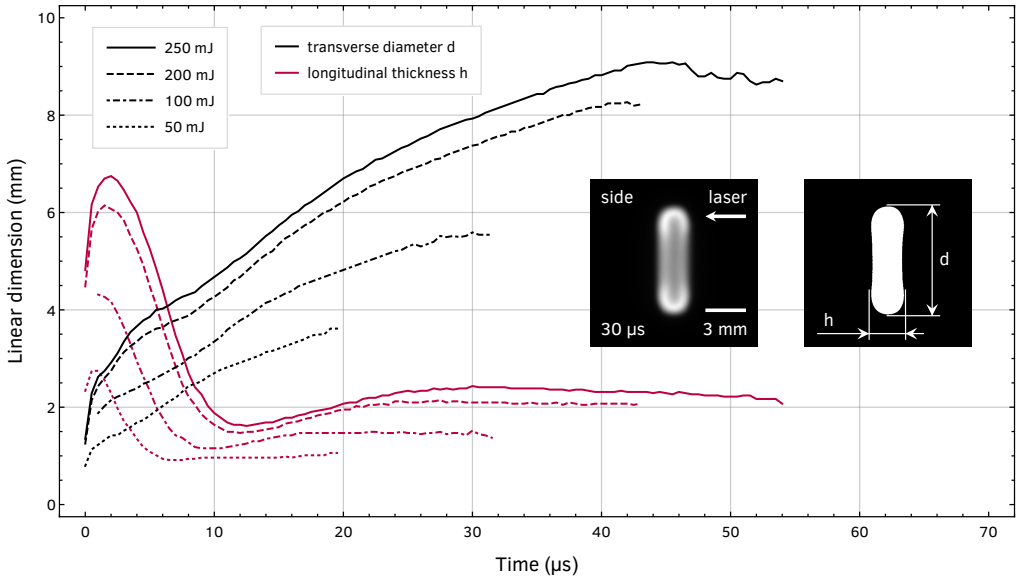

Figure 2.8: Linear dimensions of a laser-generated toroidal plasma for laser pulse energies of 50, 100, 200, and 250 mJ. This graph shows the transverse diameter (orthogonal to the laser propagation direction) and longitudinal thickness of the axis-oriented smallest bounding box of the side view images after binarisation by cluster variance maximization (Otsu's algorithm). The inset shows a typical toroidal plasma and its binarised image together with the definitions for transverse diameter and longitudinal thickness. This graph is based on the same recordings as those used for figures 2.4–2.6.

60 µs — The toroidal plasma dissolves and is no longer visible. This does not necessarily mean that a quiescent state has been reached, gas flow may still be present.

The spectral radiant intensity[38] of the plasma during its evolution is presented in figure 2.9. As noted in the beginning of this section, the quantitative measurements have been captured through a bandpass filter enclosing the atomic helium emission lines at 587.6 nm. It is remarkable, consideration the huge change in size and morphology of the plasma, that the radiant intensity decreases purely exponentially. Moreover, two exponential sections can be observed, where the second section is decreasing even faster than the first. In section 2.5 we link this increase in the exponential decay rate to the restored density in the surrounding area of the toroidal plasma.[39]

To conclude this section, we present in figure 2.10 a series of images showing that the generation of a toroidal plasma is robust over a wide range of laser pulse energies. We presumed that a comparable moment in the evolution of a toroidal plasma is the intersection of the two fitted

[38] Spectral radiant intensity is defined as the energy emitted per unit time per unit solid angle per unit wavelength.

[39] Oxygen impurities due to the contamination of our plasma reactor also affects the decay rate. See section 2.6 for details.

exponential sections of the spectral radiant intensity shown in figure 2.9. The similar morphology of the images at these moments confirms that this intersection is indeed a comparable moment in the evolution of a toroidal plasma. The apparent relation between laser pulse energy and time will become clearer in section 2.5.

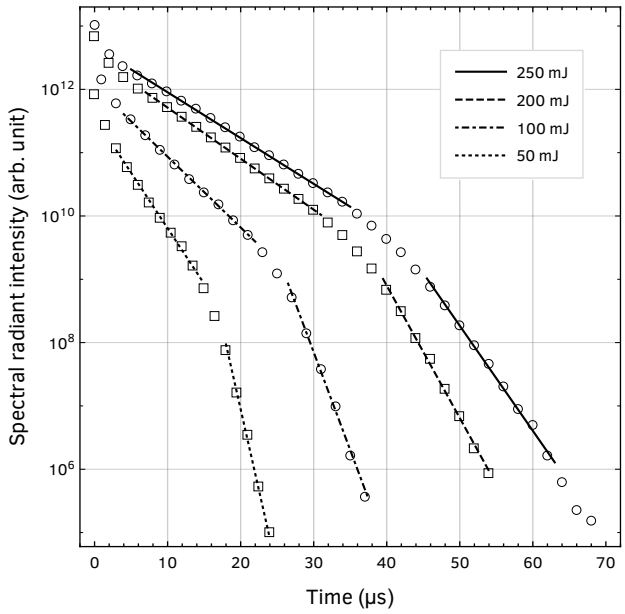

Figure 2.9: Spectral radiant intensity of a laser-induced breakdown plasma created with a pulse energy of 50, 100, 200, and 250 mJ. Measurements have been recorded at a 500 ns interval but for clarity fewer are shown (markers). Purely exponential decay is visible for both sections of the spectral radiant intensity curve. Each section has been fitted to an exponential (line segments). Note the different time span compared to figure 2.7. This graph is based on the same recordings as those used for figures 2.4–2.6.

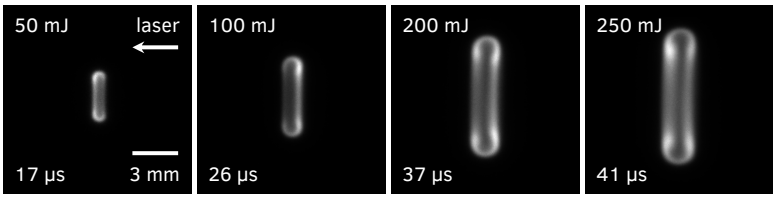

Figure 2.10: Toroidal plasmas generated with a pulse energy of 50, 100, 200, and 250 mJ. The images show that the generation of a toroidal plasma is robust over a wide range of laser pulse energies. The images are from a comparable moment in the evolution of a toroidal plasma (see text for details) and are based on recordings captured using similar experimental settings as those presented in figures 2.4–2.6.

2.4 *Numerical Abel inversion using transform techniques*

In the previous section we presented a self-organising toroidal plasma emerging solely due to a single laser-induced breakdown plasma. We attributed the generation of this toroidal structure to fluid flow along the symmetry axis of the plasma. Useful for the visualisation of this fluid flow is a three-dimensional tomographic reconstruction of the toroidal plasma. This section presents a novel numerical method, based on transform techniques for the Abel inversion,[40] that will be used to perform this reconstruction.

[40] Hutchinson 2002, p. 141; Hanson 1993; Dribinski et al. 2002; Pretzler et al. 1992; Smith et al. 1988.

A three-dimensional tomographic reconstruction is feasible because of two characteristics of our toroidal plasma that are helpful to us. It has been noted before that our toroidal plasmas are optically thin plasmas. This means that the observations we make, and the images we record, are two-dimensional projections of the three-dimensional toroidal plasma. Moreover, if we concentrate on the side view images, recorded orthogonal to the symmetry axis of the toroidal plasma, we can appreciate the fact that these images are projections of an axially symmetric object, owing to the symmetrical nature of our experiment. These characteristics provide the necessary conditions[41] to employ Abel inversion and obtain a three-dimensional tomographic reconstruction.

[41] Cooper 1966, p. 96.

If we assume that the symmetry axis is oriented horizontally with respect to the recorded images, each column of these images originates from the projection of a slice through the toroidal plasma, obtained orthogonal to its symmetry axis.

Figure 2.11: Schematic of the poloidal plane of a toroidal object (shown as a torus) as used in this work.

Let the symmetry axis coincide with the z-axis and let $f(x,y,z)$ be the radiant intensity distribution. Then axial symmetry implies

$$f(x,y,z) = f(r,z)$$

where $f(r,z)$ represents the poloidal radiant intensity profile of our toroidal plasma (see figure 2.11), $r^2 = x^2 + y^2$, and z labels the aforementioned slice through the toroidal plasma. The projection $p(x,z)$ of the toroidal plasma onto the x-axis is given by

$$p(x,z) = \int_{-\infty}^{\infty} f(x,y,z)\,\mathrm{d}y$$

or, using axial symmetry, by

$$p(x,z) = 2\int_{|x|}^{\infty} f(r,z)\frac{r}{\sqrt{r^2-x^2}}\,\mathrm{d}r \tag{2.1}$$

which is the Abel transform[42] of $f(r,z)$. Note that the projection $p(x,z)$

[42] Cooper 1966, p. 96–97; Abel 1826; Arfken et al. 1995, p. 929.

represents the side view image recorded by our ICCD camera. In order to reconstruct the poloidal radiant intensity profile $f(r,z)$ we need to invert, for every slice z, the projection $p(x,z)$.

Let $p(x,z) \equiv p(x) \equiv p$ and $f(r,z) \equiv f(r) \equiv f$ to emphasise that the inversion is performed slicewise and let $\widehat{A}$ be the Abel transform operator. Then we may write equation 2.1 as

$$p = \widehat{A} f. \tag{2.2}$$

The direct inversion of the Abel transform[43] involves the derivative of the projection p and is therefore rather sensitive to experimental noise in the recorded images.[44] Several techniques exist that mitigate this problem,[45] including the projection slice theorem.[46,47] In the presence of circular symmetry, the projection slice theorem reduces to a basic theorem relating the Abel, Fourier and Hankel transforms[48]

$$\widehat{H}\widehat{F}\widehat{A} = \widehat{I} \tag{2.3}$$

where $\widehat{H}$, $\widehat{F}$, and $\widehat{A}$ are respectively the zero-order Hankel, Fourier, and Abel transform operators, and $\widehat{I}$ is the identity operator. Written as an integral equation in g we have

$$\int_0^\infty \mathrm{d}k\, \mathrm{J}_0(\alpha k) k \;\; \frac{1}{2\pi} \int_{-\infty}^{\infty} \mathrm{d}x\, \mathrm{e}^{-\mathrm{i}kx} \;\; 2\int_{|x|}^{\infty} \mathrm{d}r \, \frac{r}{\sqrt{r^2 - x^2}} \;\; g(r) = g(\alpha)$$

where J_0 is the zero-order Bessel function of the first kind.[49] The zero-order Hankel, Fourier, and Abel transforms are readily identified.[50,51,52]

The Hankel transform is computationally challenging,[53] but if we realise that the Hankel transform is reciprocal,[54] that is, $\widehat{H}\widehat{H} = \widehat{I}$, we can deduce from equation 2.3 that

$$\widehat{F}\widehat{A}\widehat{F}\widehat{A} = \widehat{I}$$

and, therewith we may write equation 2.2 as

$$f = \widehat{F}\widehat{A}\widehat{F} p \tag{2.4}$$

providing a novel theorem for the inversion of the Abel transform, readily calculable using the following numerical methods. Note that the Abel transform assumes circular symmetry, deviations thereof affect the inversion.[55]

The Fourier transform can be calculated using the following method. Let the sequence $\{p_n\}_{n\in\mathbb{Z}}$ be a discrete representation of a projection p. By definition the sequence $\{p_n\}$ is even in n, consequently the discrete

[43] Cooper 1966, p. 96.

[44] Griem 1997, p. 241; Hutchinson 2002, p. 143; Dribinski et al. 2002.

[45] Smith et al. 1988; Dribinski et al. 2002; Pretzler 1991.

[46] Bracewell 1956.

[47] The projection slice theorem, a fundamental relation in computed tomography, relates a one-dimensional slice of a two-dimensional Fourier transform to a one-dimensional Fourier transform of a one-dimensional projection.

[48] Bracewell 1956, p. 209.

[49] Arfken et al. 1995, p. 632.

[50] Arfken et al. 1995, pp. 846, 852; Bracewell 1956, p. 206.

[51] The connection to the projection slice theorem is revealed by realising that the Hankel transform is identical to the two-dimensional Fourier transform of a radially symmetric function.

[52] The applied Fourier transform uses the quantum mechanical sign convention, where a wave propagating in the $\boldsymbol{k}$ direction for $\omega > 0$ is represented by $e^{i\boldsymbol{k}\cdot\boldsymbol{x} - i\omega t}$.

[53] Candel 1981.

[54] Arfken et al. 1995, p. 648; Bracewell 1956, p. 207.

[55] Smith et al. 1988; Pretzler et al. 1992.

Fourier transform $\{f_k\}_{k\in\mathbb{Z}}$ of $\{p_n\}$ is even in k. If we assume that the subsequence $\{p_n\}_{n\geq 0}$ has length $N \in \mathbb{N}$, the discrete Fourier transform can be calculated using the type-I discrete cosine transform[56] given by

$$f_k = \frac{1}{2N-2}\left[p_0 + (-1)^k\, p_{N-1} + 2\sum_{n=1}^{N-2} p_n \cos\left(\frac{\pi}{N-1}kn\right)\right].$$

[56] A discrete cosine transform has the advantage that it is guaranteed to be real valued.

The Abel transform can be calculated using the following method. Let the sequence $\{f_k\}_{k\in\mathbb{Z}}$ be an even sequence in k and assume that the subsequence $\{f_k\}_{k\geq 0}$ has length $N \in \mathbb{N}$. The discrete Abel transform $\{p_n\}_{n\in\mathbb{Z}}$ of $\{f_k\}$ can be calculated using the direct summation

$$p_n = \sum_{m=-N+1}^{N-1} \widetilde{f}\left(\sqrt{n^2+m^2}\right)$$

where $\widetilde{f}$ is an interpolation of the sequence $\{f_k\}$. For our tomographic reconstruction a third order polynomial interpolation will be used.

2.5 *Tomographic reconstruction and flow experiments*

In the previous sections we introduced a self-organising toroidal plasma emerging solely by virtue of a single laser-induced breakdown plasma. We attributed the generation of this toroidal structure to fluid flow along the symmetry axis of the plasma. This fluid flow can be interpreted as flow repleting a low density cavity, created in the wake of the shock generated by the breakdown plasma.

The existence of this cavity will be confirmed in section 3.2 where we present high-speed Schlieren images visualising the shock, and show that, because of the presence of this low density cavity, the creation of a laser-induced breakdown plasma will be suppressed in experiments with successive laser pulses.

Useful for the visualisation of the aforementioned fluid flow is a three-dimensional tomographic reconstruction of the toroidal plasma. In this section we present the poloidal radiant intensity profile[57] of our toroidal plasma, obtained through such a reconstruction, and infer the fluid flow from the motion of the plasma emission in the poloidal plane.

[57] See figure 2.11 for a schematic of the poloidal plane of a toroidal object as used in this work.

The characteristic time scale of the dynamics involved is explained by an intuitive model based on elementary thermodynamic principles. In conclusion, we will present flow experiments with a deliberately broken symmetry, confirming our hypotheses on the generation of the toroidal structure.

Tomographic reconstruction

A three-dimensional tomographic reconstruction of the toroidal plasma is feasible because of two helpful characteristics. We noted before that the toroidal plasmas are axially symmetric and optically thin plasmas. Moreover, we explained in section 2.4 that these characteristics provide the necessary conditions to employ Abel inversion[58] and to obtain a poloidal radiant intensity profile of the toroidal plasma.

[58] Cooper 1966, p. 96.

Figure 2.12 presents the evolution of the poloidal radiant intensity profile, showing the development and subsequent dissolvement of the toroidal plasma. These images have been obtained by Abel inversion[59] of the individual columns of the recorded side view images presented in figure 2.5. To assess whether the reconstruction is trustworthy, we compare, in the same figure, the poloidal radiant intensity profile with the corresponding front view images. We see that in the toroidal phase a dark region is noticeable in the centre of the front view images, which is confirmed by the dark region around the symmetry axis in the tomographically reconstructed images.

[59] The Abel inversion has been calculated using equation 2.4 and the numerical methods outlined in section 2.4.

The symmetry axis itself is highly sensitive to noise arising from a nearly singular condition in the reconstruction. This can be understood intuitively from the fact that the contribution from annuli near the symmetry axis is small compared to the contribution from annuli at larger distances.[60] This manifests itself in an accumulation of noise near the symmetry axis in the reconstructed images. To suppress artefacts arising from this noise, the one pixel wide symmetry axis has been

[60] Hanson 1993, p. 694; Griem 1997, p. 241.

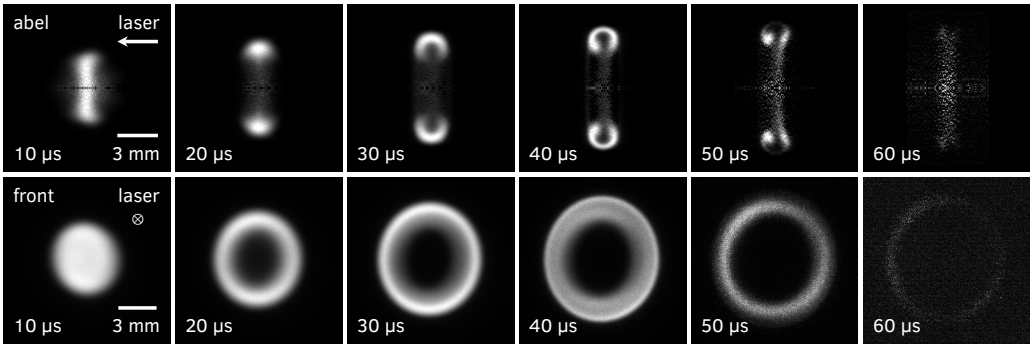

Figure 2.12: Evolution of the poloidal radiant intensity profile of a laser-generated toroidal plasma (top row) obtained through a three-dimensional tomographic reconstruction using the images presented in figure 2.5, together with the corresponding front view images (bottom row) to assess the reliability of the tomographic reconstruction. The front view images are identical to those shown in figure 2.6 and show slightly oval plasma structures due to a necessary skewed viewing direction. The images have been captured at increasing times (left to right) after the breakdown laser pulse. Note that the images have been individually normalised to their maximum intensity to respect the large dynamic range in intensity of the entire evolution. The images are based on the same recordings as those used for figures 2.4–2.6.

blackened in the reconstructed images. This is most visible at 10–15 µs.

Because the Abel inversion outlined in section 2.4 must be applied to an even sequence, the recorded side view images were symmetrised by discarding the top half of each image, to then apply the Abel inversion to the individual columns of the remaining bottom half. This geometrically motivated symmetrisation can be improved[61] by a precise calculation of the position of the symmetry axis.

[61] Pretzler et al. 1992.

Fluid flow visualisation

For the visualisation of the fluid flow responsible for the development of the toroidal plasma, we present in figure 2.13 contrast enhanced false colour images that better visualise the core of the toroidal plasma. To

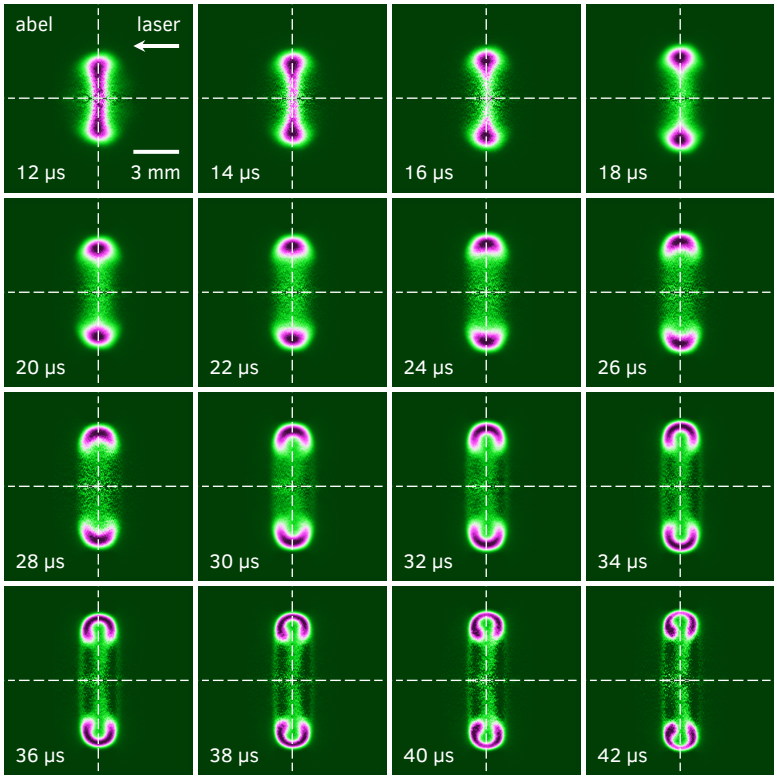

Figure 2.13: Fluid flow responsible for the development of a toroidal plasma. The contrast enhanced false colour images have been obtained through a three-dimensional tomographic reconstruction of the toroidal plasma and clearly visualises its core (purple). The fluid flow is inferred from the motion of the plasma emission. The longitudinal compression initially forming the plasma pillbox completely pinches off its centre at 18 µs thereby generating a toroidal plasma structure (see text for details). The images have been captured at increasing times after the breakdown laser pulse. Note that the images have been individually normalised to their maximum intensity to respect the large dynamic range in intensity of the entire evolution. The images are based on the same recordings as those used for figures 2.4–2.6.

assess whether the false colour images introduce artefacts or distort the images, we compare in figure 2.14, selected false colour images with their original and reconstructed black and white images. The images are consistent and do not show unexpected behaviour. Note however that the contrast enhanced images show slightly larger plasma structures than the black and white images. This comparison also nicely illustrates the necessity to perform a tomographic reconstruction, in order to observe features that are unobservable in the original images.

Figure 2.13 shows that the longitudinal compression forming the plasma pillbox mentioned in section 2.3 continues along the symmetry axis of the plasma structure (the symmetry axis is represented by the horizontal dashed line in the images). Eventually, at 18 µs, the squeezing fluid flow, which at the same time repletes the aforementioned low density cavity, completely pinches off the centre of the plasma pillbox, thereby generating a toroidal plasma. Moments later, around 20–22 µs, we observe an almost perfect plasma torus.

Due to our highly symmetrical breakdown plasma, the squeezing fluid flow that approaches the plasma from both sides is of approximate equal strength. These fluid flows will collide in the centre of the toroidal

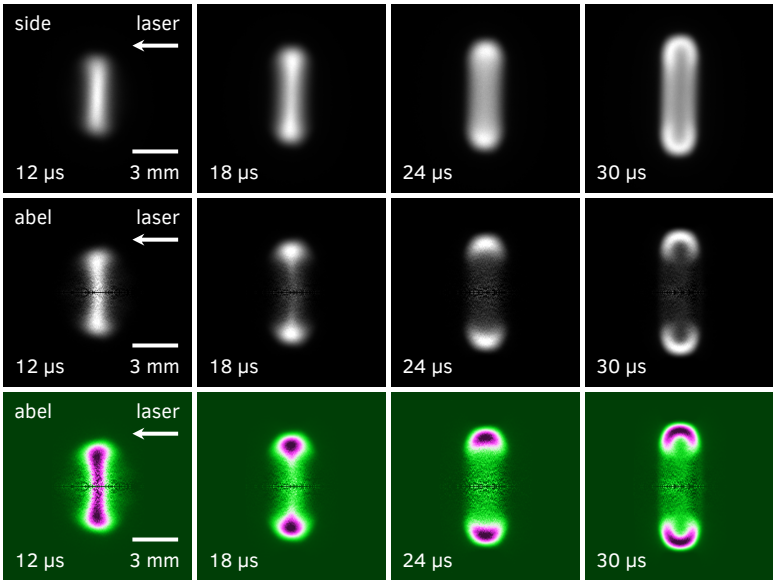

Figure 2.14: Comparison of selected contrast enhanced false colour images of the tomographically reconstructed, poloidal radiant intensity profile (bottom row) with the corresponding black and white (centre row) and original side view images (top row) to assess whether the false colour images introduce artefacts or distort the images. The false colour images (bottom row) are identical to those shown in figure 2.13. This comparison also illustrates the necessity to perform a three-dimensional tomographic reconstruction, in order to observe subtle features that are unobservable in the original side view images.

plasma, and spread out into the symmetry plane orthogonal to the symmetry axis, thereby pushing the plasma outward. This flow becomes visible from 24 µs onward, and deforms and erodes the toroidal plasma even further. This manifests itself as a horseshoe shaped plasma in the poloidal radiant intensity profile.

An estimate of the speed of the aforementioned fluid flow is easily obtained from the presented images. When we consider the fluid flow in the plane orthogonal to the symmetry axis, in the images between 24 µs and 42 µs, a fluid flow speed of 95 ± 3 m/s is obtained.

To interpret this speed it is helpful to compare it with the speed of sound in a gas, or more aptly, with the mean thermal speed of its constituents given by[62,63]

[62] Jeans 1940, p. 42.

[63] Note that these speeds are of the same order of magnitude, see Jeans 1940, p. 57.

$$v = \sqrt{\frac{8}{\pi}\frac{kT}{m}} \tag{2.5}$$

where k is the Boltzmann constant, T the gas temperature, and m the mass of an atom or molecule of the gas. Substitution of tabulated values[64] for helium at a temperature of 300 K results in a mean thermal speed of 1260 m/s.

[64] Haynes 2014.

The observed fluid flow speed is therefore approximately one tenth of the mean thermal speed. Since, by then, the toroidal plasma is fairly developed, the density in its centre has been partially restored as a result of the repleting fluid flow.[65] So the observed fluid flow does not expand into vacuum, but into a region with a partially restored density. The reduced fluid flow speed therefore seems reasonable. At earlier times, the fluid flow is not visible, but its speed will be higher because the density in the centre of the toroidal plasma is still reduced.

[65] The number density by that time is approximately 0.7 n_0. See figure 2.17 for details.

Characteristic time scale

So far we have presented a tomographically reconstructed poloidal radiant intensity profile that ably visualises the fluid flow responsible for the development of the toroidal plasma, and found that the flow speeds involved are akin to the mean thermal speed of the helium atoms. The observed characteristic time scale for the development of the toroidal plasma can be explained by following on from the foregoing through a simple model based on elementary thermodynamic principles.

Although this model will provide a characteristic time scale at which structure is expected to develop, it will not explain the mechanisms responsible for the development of the toroidal plasma. The asymmetric fluid flow necessary for this structure will be addressed in section 3.3.

To model the evolution of a low density cavity, created in the wake of a shock generated by a laser-induced breakdown plasma, we assume that the volume of the breakdown plasma is infinitesimally small and that the laser pulse energy as a whole is converted to kinetic energy of the fluid surrounding the breakdown plasma.[66] Moreover, following on from our assumption that this model will not explain structure formation, we assume that the work done on the fluid is spherically symmetric in nature.

[66] For laser pulse energies well above breakdown threshold, over 85% of the energy will be absorbed by the breakdown plasma, see Harilal et al. 2015; Y. Chen et al. 2000.

Inevitably a low density cavity will form, which continues to expand until all kinetic energy of the fluid is converted to potential energy of the cavity. At this stage the fluid is motionless. If we then assume that the successive repletion of the cavity is solely dictated by the thermal motion of the constituents of the fluid[67] we can infer a characteristic time scale by dividing the extremum of the radius of the cavity by the mean thermal speed of the constituents of the fluid. The evolution portrayed is illustrated in figure 2.15 and can be expressed mathematically as follows.

[67] This obviously is a coarse but nevertheless insightful approximation. A better one based on fluid dynamics has already been found by Besant 1859, p. 170 and Rayleigh 1917. See also Sinibaldi et al. 2019.

Let E be the laser pulse energy and assume that it as a whole is converted to work done on a fluid with ambient pressure p. Moreover, assume that the volume of the breakdown plasma is infinitesimally small and that the work $p\,\mathrm{d}V$ done on the fluid is spherically symmetric in nature. Then we may write

$$E = \int p\,\mathrm{d}V = \frac{4}{3}\pi R^3\,p$$

where R is the extremum of the radius of the low density cavity.

Let τ be the characteristic time scale, defined as the time between breakdown and the collapse of the cavity, and further assume that the expansion and repletion are of equal duration. Then we have

$$\tau = 2\,\frac{R}{v}$$

where v is the mean thermal speed defined by equation 2.5. Using the

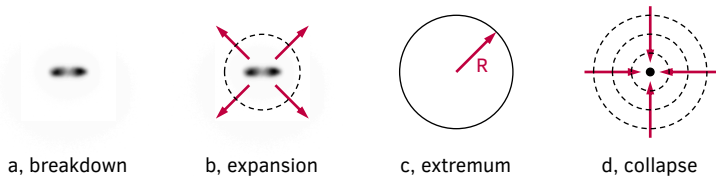

Figure 2.15: Schematic of the evolution of a low density cavity generated by a laser-induced breakdown plasma. The evolution of the cavity can be differentiated into four phases: breakdown, expansion, extremal radius, and collapse (see text for details). The repleting fluid flow is responsible for the generation of the toroidal plasma and dictates a characteristic time scale in the development of its structure.

equation of state $p/\rho = kT/m$ for an ideal gas[68,69] the characteristic time scale τ may be written as

$$\tau = \frac{1}{2}\sqrt[3]{3}\left(\frac{\pi}{2}\right)^{\frac{1}{6}} E^{\frac{1}{3}}\rho^{\frac{1}{2}}p^{-\frac{5}{6}}$$

where ρ is the mass density of the fluid. Substitution of tabulated values[70] for helium at a temperature of 300 K results in a characteristic time scale of 13.4 µs for a laser pulse energy of 250 mJ. This is in agreement with the observations presented in figure 2.13 where at 16 µs the repleting fluid flow approaches the symmetry plane orthogonal to the symmetry axis.

The calculated time scale is lower than observed experimentally because, as explained earlier, the observed fluid flow speed is lower than the mean thermal speed. The difference we find here is smaller than in the previous subsection because this value has been obtained at an earlier moment in the evolution, when the density in the cavity was restored to a lesser extent.

Density of helium atoms in the centre of the toroidal plasma

The characteristic time scale just obtained can be confirmed by a measurement of the evolution of the number density in the centre of the toroidal plasma. Using a second laser-induced breakdown plasma as a probe, created using an additional high power Nd:YAG laser, the spectral radiant intensity of this breakdown plasma can be used as a measure of the local number density, when correlated with calibration measurements separately obtained in quiescent helium gas at known number densities. Figure 2.16 presents selected images that illustrate this probing with a second laser-induced breakdown plasma.

The evolution of the number density in the centre of the toroidal plasma, obtained in the above manner, is presented in figure 2.17, and

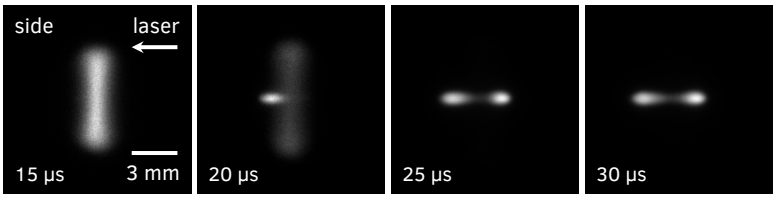

Figure 2.16: Second laser-induced breakdown plasma used to measure the number density in the centre of the toroidal plasma. (15 µs) Toroidal plasma with indiscernible (suppressed) second breakdown plasma. (20 µs) Visible second breakdown plasma with faintly visible toroidal plasma. (25 and 30 µs) Clearly visible second breakdown plasma, with toroidal plasma too faint to discern. Note that the images have been individually normalised to their maximum intensity. The images are based on the same recordings as those used for figure 2.17.

[68] Landau et al. 1987, p. 318.

[69] Note that T is the temperature of the ambient fluid.

[70] Haynes 2014.

shows that the number density starts to replete within 20 µs after the breakdown laser pulse. This is in agreement with the model presented in the previous section. Unfortunately, the measurements obtained at earlier times are not reliable due to the presence of the bright plasma pillbox, which interferes with the measurement of the intensity of the probing breakdown plasma.

A notable observation can be made regarding the time-dependent exponential decay rate of the spectral radiant intensity of the toroidal plasma. As already noted in section 2.3, two exponential sections can be observed, where the second section is decreasing even faster than the first. This has already been observed in figure 2.9, but is likewise visible in figure 2.17.

The time-dependent decay rate presented in figure 2.17 shows that, at approximately 30 µs the decay rate starts to increase rapidly. This is roughly 10 µs later than when the density in the centre of the toroidal plasma starts to increase. Note that in this figure, the region where the measurement noise becomes prominent, indicated by a decrease in the

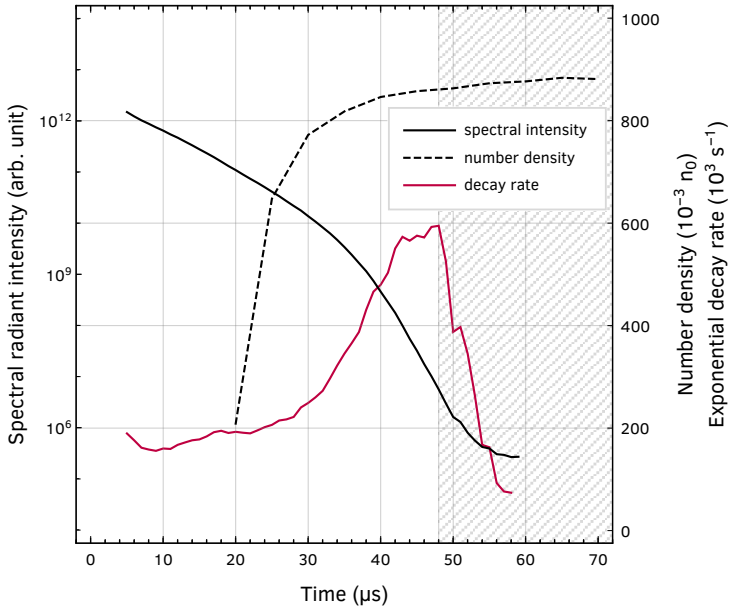

Figure 2.17: Number density in the centre of the toroidal plasma (dashed line) measured using a second laser-induced breakdown plasma as a probe. The number density starts to increase at approximately 20 µs as a result of the repleting fluid flow responsible for the generation of the toroidal plasma. Note the (delayed) correlation between the increase in the time-dependent exponential decay rate (purple line) of the spectral radiant intensity curve (black line) and the increase in number density. The region where the measurement noise becomes prominent is indicated by a grey shading. This graph is based on recordings captured using similar experimental settings as those presented in figures 2.4–2.6. Loschmidt constant $n_0 = 2.65\ 10^{25}\ \mathrm{m}^{-3}$ is the number density of an ideal gas at standard temperature and pressure.

time-dependent decay rate, is highlighted by a grey shading.

The delayed increase in the decay rate can be understood by realising that the density measurements are performed at the symmetry axis, in the centre of the toroidal plasma, while the time-dependent exponential decay rate is derived from the spectral radiant intensity of the toroidal plasma, originating from a considerable distance from the symmetry axis. This is likewise confirmed by observing that the poloidal radiant intensity profile of the toroidal plasma, presented in figure 2.13, clearly starts its deformation into a horseshoe shaped plasma precisely when the decay rate starts to increase.

Flow experiment with a deliberately broken symmetry

Until now we have argued that, as a result of the highly symmetrical nature of our laser-induced breakdown plasma, the repleting fluid flow responsible for the development of the toroidal plasma, approaches the plasma from both sides equally. However, even though the breakdown plasma presented in figure 2.4 appears very symmetric, it in fact is not. This can be appreciated from the slight asymmetry visible in the poloidal radiant intensity profile presented in figure 2.13, where the asymmetry is most clearly visible from 38 µs onward.

When a toroidal plasma is generated with a different laser pulse energy, this asymmetry is likewise observed, albeit occasionally reflected in the symmetry plane. This alternating asymmetry is clearly visible in figure 2.18. A slight imbalance in the generation of a laser-induced breakdown plasma appears to results in a slightly asymmetric fluid flow repleting the low density cavity.

To confirm our interpretation regarding the symmetric repletion of the low density cavity, by the fluid flow responsible for the development of the toroidal structure, we performed flow experiments where the

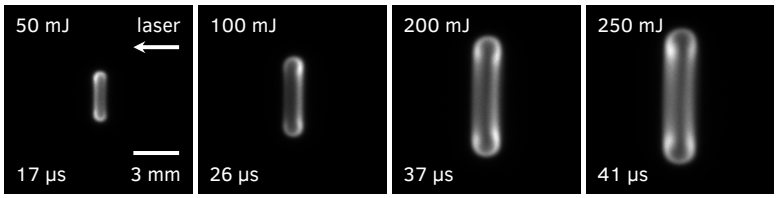

Figure 2.18: Slight asymmetry visible in the symmetry plane orthogonal to the symmetry axis of a toroidal plasma due to an imbalance of the fluid flow responsible for its development. The toroidal plasmas have been generated with a pulse energy of 50, 100, 200, and 250 mJ and show an alternating asymmetry with different laser pulse energies. The images are based on recordings captured using similar experimental settings as those presented in figures 2.4–2.6 and are a reproduction of figure 2.10.

symmetry in the plane orthogonal to the symmetry axis is deliberately broken. This symmetry breaking has been realised by placement of a metal sheet close to the laser focus, through which the laser pulse is allowed to pass, through a small 2.8 ± 0.1 mm hole. The distance of the metal sheet to the laser focus was 6.0 ± 0.1 mm, sufficient to avert contact with the focussed laser pulse.

The poloidal radiant intensity profile, again obtained through a three-dimensional tomographic reconstruction of the toroidal plasma, is presented in figure 2.19. In figure 2.20 selected contrast enhanced false colour images are presented, together with the original and reconstructed black and white images, to assess whether the false colour images introduce artefacts in the reconstructed images. This comparison

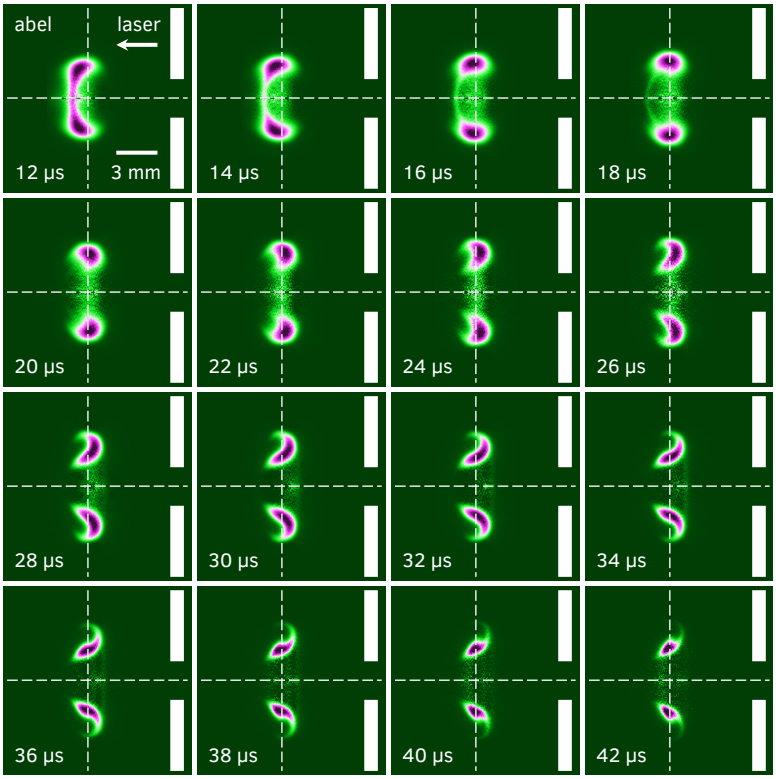

Figure 2.19: Development of a toroidal plasma with a deliberately broken symmetry by means of a metal sheet (two white rectangles) close to the laser focus. The metal sheet has a 2.8 mm hole through which the laser pulse passes and is shown to scale. The fluid flow is inferred from the motion of the plasma emission. Note the revolving motion of the plasma core (purple) testimonial to the presence of vorticity. The contrast enhanced false colour images have been obtained through a three-dimensional tomographic reconstruction of the toroidal plasma. The images have been captured at increasing times after the breakdown laser pulse. Note that the images have been individually normalised to their maximum intensity to respect the large dynamic range in intensity of the entire evolution. The images are based on recordings captured using similar experimental settings as those presented in figures 2.4–2.6.

once more illustrates the necessity to perform a three-dimensional tomographic reconstruction in order to observe subtle features that are unobservable in the original images.

Note that in the presented images we have depicted the metal sheet to scale as two white rectangles. The symmetry axis is represented by the horizontal dashed line, while the vertical dashed line is identical to the aforementioned symmetry plane orthogonal to the symmetry axis. Both dashed lines cross at the laser focus in the centre.

The detailed evolution of the poloidal radiant intensity profile can best be understood by anticipating the consequences of the placement of the symmetry breaking metal sheet. When we consider the expanding low density cavity from our model presented earlier in this section, we can expect that the expansion along the symmetry axis will be obstructed by the symmetry breaking metal sheet. This obstruction prevents the low density cavity to extend beyond the metal sheet. Consequently, we expect that the repleting fluid flow from beyond the metal sheet, flowing through the small 2.8 mm hole, will commence in advance with respect to the repleting flow due to the collapse of the cavity. Due to this asymmetry, the two repleting flows are expected to

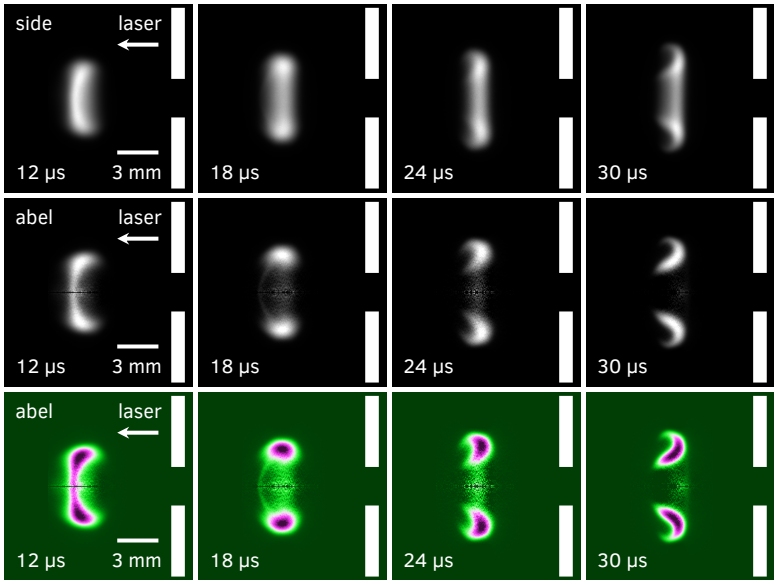

Figure 2.20: Comparison of selected contrast enhanced false colour images of the tomographically reconstructed, poloidal radiant intensity profile (bottom row) and the corresponding black and white (centre row) and original side view images (top row) to assure the false colour images do not introduce artefacts or deform the original images. The false colour images (bottom row) are identical to those shown in figure 2.19. This comparison again illustrates the necessity to perform a three-dimensional tomographic reconstruction in order to observe subtle features that are unobservable in the original images.

collide, not in the centre of the toroidal plasma, as in figure 2.13, but further away from the metal sheet. Accordingly, the flow is expected to spread out, not in the symmetry plane of the original experiment, which is represented by the vertical dashed line in figure 2.19, but at a distance to that plane.

Our foregoing anticipation is confirmed by the evolution presented in figure 2.19. The plasma pillbox is seen to be pushed aside due to the fluid emanating from the hole in the metal sheet. The same fluid flow subsequently pushes a hole into the plasma pillbox, which at 16 µs, a few microseconds earlier than in our symmetric experiment presented in figure 2.13, completely pierces through the centre of the plasma pillbox, thereby again forming a toroidal structure.

The colliding fluid flows are difficult to distinguish in the beginning, but start to appear at 22 µs as a distinct notch in the poloidal profile. This notch corresponds to the earlier observed horseshoe shaped plasma in the original experiment. We see that the fluid flow is not spreading out into a plane, but instead into a cone. This can be expected because the fluid flow repleting the cavity has a larger extent than the fluid flow emanating through the hole in the metal plate.

Lastly, as a result of the colliding fluid flows, the toroidal plasma is observed to rotate. This is a testimony of the presence of vorticity. Numerical studies on the fluid dynamical effects of laser energy deposition have shown[71] that the generation of vorticity found in these systems stems from the asymmetry of the breakdown plasma, whereas in our case the origin lies in the asymmetric experimental setting.

[71] Ghosh et al. 2008; Morsy et al. 2002.

Plasma flow through a toroidal plasma

In one of our preliminary experiments, we utilised the ability of our experimental set-up to create a second laser-induced breakdown plasma in close proximity of a previously generated toroidal plasma. This has been realised by displacing the focus of the laser pulses of a second Nd:YAG laser, using a diverging plano-concave lens as explained in the experimental details in section 2.2.

Figure 2.21 presents selected images of the evolution of a second laser-induced breakdown plasma, created in close proximity of a toroidal plasma which is in development at that time. In each image, a side view (top half) and a slightly skewed front view (bottom half) are presented simultaneously. The principal laser-induced breakdown plasma, which develops into the toroidal plasma, is shown in green false colour in the first two images, to be able to distinguish it from the second

breakdown plasma. Note that in the second image, at 8.1 µs, the toroidal plasma is very faint, to make it visible it has been combined with a separately obtained green false colour image of the toroidal plasma.

First, a laser-induced breakdown plasma is created at 0 µs. Then, 8 µs later, while the toroidal plasma is still in development, a second laser-induced breakdown plasma is created by the second Nd:YAG laser. This second breakdown plasma is created with reduced power, to still be able to observe the toroidal plasma that is steadily decreasing in intensity.

From the evolution presented in figure 2.21, it is clear that the second breakdown plasma is drawn through the centre of the toroidal plasma generated by the principal breakdown plasma. This attests to fluid flow through the centre of the toroidal plasma, and implies that the low density cavity responsible for the generation of the toroidal structure, repletes in an asymmetric way. This can be understood when

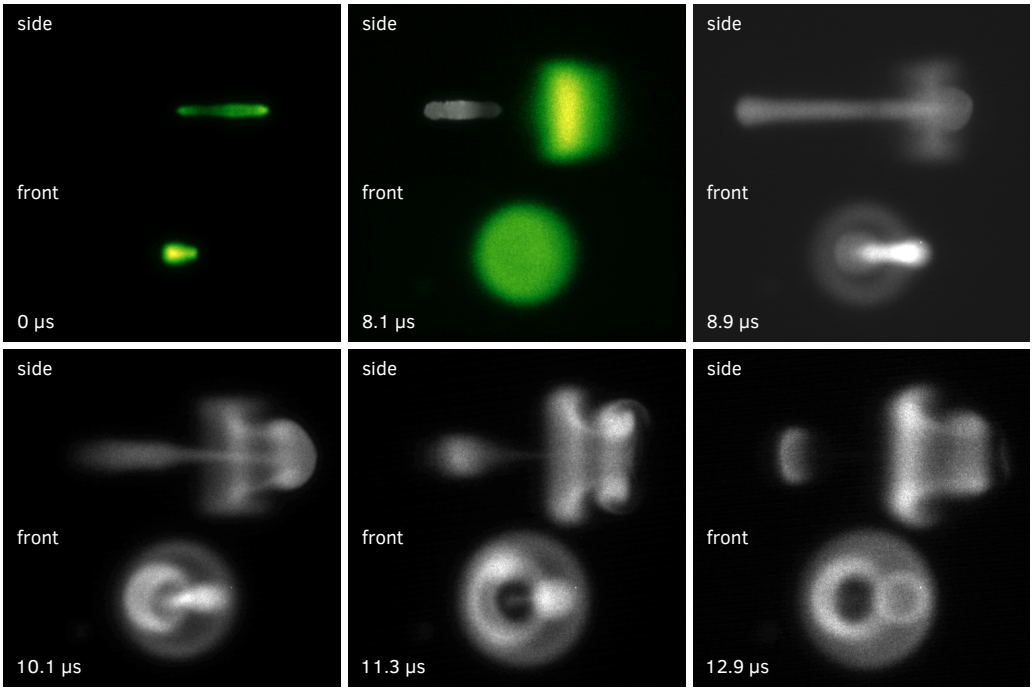

Figure 2.21: Selected images of the evolution of a second laser-induced breakdown plasma, created at 8 µs, and in close proximity of a toroidal plasma which is in development at that time. In each image, a side view (top half) and a slightly skewed front view (bottom half) are presented simultaneously. The principal laser-induced breakdown plasma, which develops into the toroidal plasma, is shown in green false colour in the first two images, to be able to distinguish it from the second breakdown plasma. Note that in the second image, at 8.1 µs, the toroidal plasma is very faint, to make it visible it has been combined with a separately obtained green false colour image of the toroidal plasma. The images have been individually normalised to their maximum intensity, and are based on recordings captured using similar experimental settings as those presented in figures 2.4–2.6.

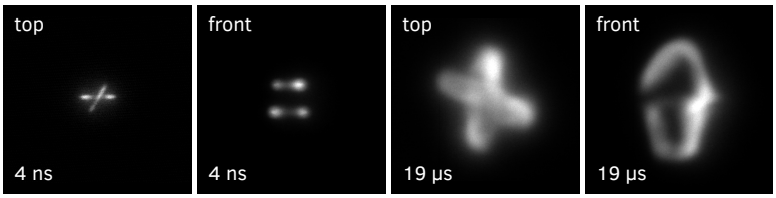

Figure 2.22: Crossed plasma arches (right pair, top and front view) developing as a result of two simultaneously created laser-induced breakdown plasmas (left pair, top and front view). The closely spaced and crossed breakdown plasmas have been created at a distance of 1.5 mm from each other therewith breaking the conventional symmetrical setting that generates a toroidal plasma.

we realise that the principal breakdown plasma presented at 0 µs is very asymmetric, and is further supported by our interpretation of the asymmetric repletion of the low density cavity presented in the previous subsection. The fluid flow along the symmetry axis is also found to have a considerable range, testified by the fact that in the last image, at 12.9 µs, three toroidal plasmas can be observed.

Experiment with two closely spaced crossed breakdown plasmas

We end this section by presenting an experiment where the symmetrical experimental setting is broken by simultaneously creating two closely spaced crossed laser-induced breakdown plasmas. This experiment was originally conducted in an attempt to create two linked toroidal plasmas, but with the insights gained in this section we can understand why we observed the two plasma arches presented in figure 2.22, instead of the naively expected linked toroidal plasmas.

We have seen that during the evolution of a single laser-induced breakdown plasma, the fluid flow repleting the low density cavity, which at the same time reshapes the breakdown plasma, predominantly manifests itself along the symmetry axis through the centre of the low density cavity. Having two closely spaced crossed breakdown plasmas, this flow will manifest itself in the plane separating these two breakdown plasmas. As a result, instead of developing into two toroidal plasmas, the two breakdown plasmas are pushed outward by the repleting fluid flow, thereby forming two separate plasma arches.

2.6 *Oxygen impurity effects in helium plasma afterglows*

In the previous sections we observed that the spectral radiant intensity of a laser-induced breakdown plasma decreases purely exponentially over the better part of its evolution. This is remarkable given the huge

change in size and morphology over time and may be indicative of local plasma chemistry.

In this regard, the contamination of our plasma reactor by oxygen impurities, as a result of the desorption of air from the reactor walls, may be a probable cause. For electrons are assumed to be responsible for the plasma emission through collisional excitation of neutral atomic helium, and the attachment of electrons to oxygen molecules is a known mechanism for removing electrons.[72] Incidentally, because of the attachment of electrons to oxygen molecules, the electron density decreases exponentially over time.

[72] Chanin et al. 1962; Raizer 1991, p. 63.

Alternative mechanisms for the decay of electrons exist, in particular recombination and ambipolar diffusion.[73] However, by recombination, the electron density decreases according to the power-law t^{-1}, and for ambipolar diffusion, the electron density decreases exponentially only when the electrons diffuse to the walls of the reactor. The latter is not likely in our experiment considering the fact that the size of our plasma is a factor 20 smaller than the diameter of our reactor.

[73] Raizer 1991, pp. 52, 60, and 67.

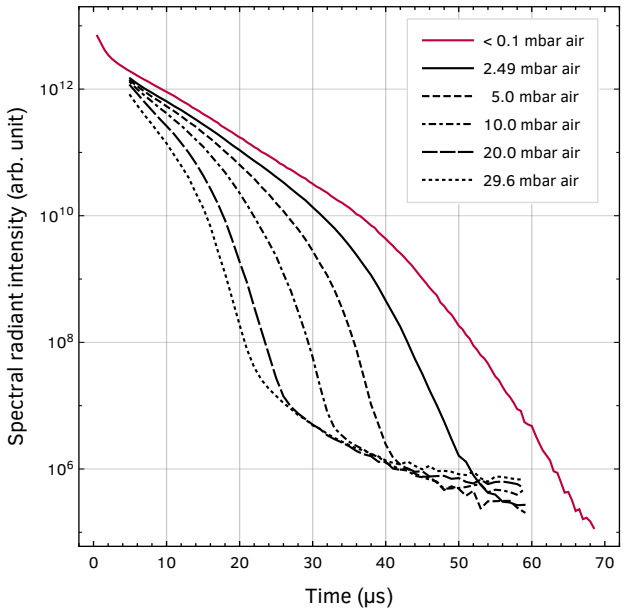

Figure 2.23: Spectral radiant intensity of a laser-induced breakdown plasma created in quiescent atmospheric pressure helium-air mixtures using a laser pulse energy of 250 mJ demonstrating the effect of contamination of our plasma reactor. The graph shows the spectral radiant intensity for different partial pressures while maintaining a total pressure of 1000 mbar. The separately obtained pure helium measurement (purple line) is identical to the 250 mJ measurement presented in figure 2.9. This graph is based on recordings captured using similar experimental settings as those presented in figures 2.4–2.6.

To examine the aforesaid hypothesis concerning the attachment of electrons to oxygen molecules, figure 2.23 presents the spectral radiant intensity of a laser-induced breakdown plasma created in quiescent atmospheric pressure helium-air mixtures, for different partial air pressures, while maintaining a total pressure of 1000 mbar. We noted before that two exponential sections can be observed, where the second section is decreasing even faster than the first. In section 2.5 we linked this increase in the time-dependent exponential decay rate to a restored density in the surrounding area of the toroidal plasma.

In figure 2.23 we also observe that, at a higher partial air pressure, the spectral radiant intensity is decreasing faster. Furthermore, we see that the instant that the exponential decay rate starts to increase, is also brought forward, implying that the fluid flow changes as well.

In figure 2.24, we present the time-dependent exponential decay rate that has been derived from the spectral radiant intensity. Clearly a plateau at 5–10 µs can be observed for all partial air pressures.

The average value of the time-dependent exponential decay rate for these plateaus is presented in figure 2.25 as a function of the partial air pressure. A linear relation can be observed between the decay rate

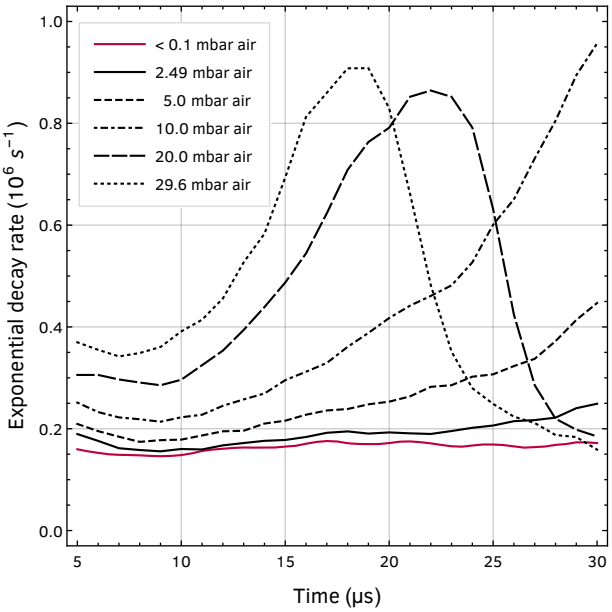

Figure 2.24: Time-dependent exponential decay rate derived from the spectral radiant intensity presented in figure 2.23. The time-dependent exponential decay rate has been calculated under the assumption of pure exponential decay between neighbouring time steps. Note the plateaus at 5–10 µs that can be observed for all partial air pressure measurements.

and the partial air pressure in the reactor. The constant contribution in this linear relation is unaccounted for and we propose that this may be caused by the slow cooling of the plasma.

For low energy electrons (< 1 eV) the attachment of electrons to oxygen molecules is primarily a three-body reaction given by[74]

[74] Chanin et al. 1962; Raizer 1991, p. 63.

$$O_2 + He + e \rightarrow O_2^- + He + \text{energy}.$$

The rate of change of the electron density may then be written as

$$\frac{dn_e}{dt} = -\lambda n_e = -k\, n_{He}\, n_{O_2}\, n_e$$

where λ is the exponential decay rate, k the three-body attachment coefficient, and n_e, n_{He}, and n_{O_2} are, respectively, the electron, helium atom, and oxygen molecule number densities. Using this relation we can validate the linear dependence presented in figure 2.25.

Let us reasonably assume that around 5–10 µs the helium number density n_{He} in the surrounding area of the toroidal plasma is not higher

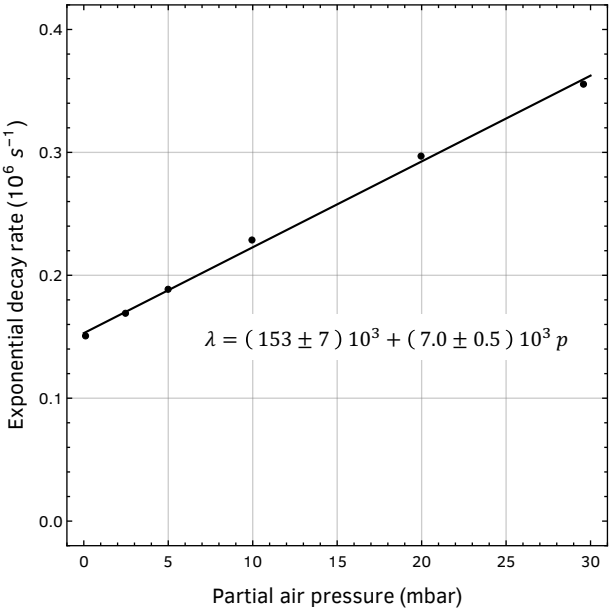

Figure 2.25: Averaged time-dependent exponential decay rate as a function of partial air pressure for the plateaus observed in figure 2.24. The time-dependent exponential decay rate of the plateaus has been fitted against a linear function (black line).

than 0.1 n_0 with n_0 the equilibrium density.[75,76] If we furthermore use $k = 2.5\ 10^{-30}\ cm^6\ s^{-1}$ as an average value for the three-body attachment coefficient[77] we find for the exponential decay rate a value of $0.11\ 10^6\ s^{-1}$ at 30 mbar partial air pressure.[78]

In figure 2.25 we see that at a partial air pressure of 30 mbar, the contribution to the time-dependent exponential decay rate originating from the presence of air in the plasma reactor is $0.21\ 10^6\ s^{-1}$. This is of the same order of magnitude as the calculated value.

The above analysis shows that the purely exponential decay of the spectral radiant intensity is, in part, attributable to the contamination of our plasma reactor by oxygen impurities. For ultra pure helium in a baked out plasma reactor we, of course, still expect the plasma to decay. The constant contribution observed in the time-dependent exponential decay rate is unaccounted for in this analysis, and we propose that this may be caused by the slow cooling of the plasma.

Although the above analysis seems fairly conclusive, it is based on a simplified model of what is in fact a complex dynamical process and might need modification. It has been shown that meta-stable and Rydberg states are present in atmospheric pressure helium afterglow plasmas.[79] Therefore, the assumed linear relationship between the neutral atomic helium emission line intensity and the electron density might need modification. In this regard, a power-law relationship has been reported in the literature.[80] Coincidentally, in this case the decay will still continue to be exponential, although with a modified decay rate. Furthermore, it has been shown that a zero dimensional kinetic model of a pure helium plasma exhibits exponential decay of the electron density,[81] which provides an explanation for the constant contribution observed in the time-dependent exponential decay rate.

[75] See figure 2.17 for details.

[76] Loschmidt constant $n_0 = 2.65\ 10^{25}\ m^{-3}$ is the number density of an ideal gas at standard temperature and pressure.

[77] Chanin et al. 1962.

[78] Note that air contains approximately 21% oxygen, see Haynes 2014.

[79] Schregel et al. 2016; Carbone et al. 2016; Nedanovska et al. 2015.

[80] Stevefelt et al. 1971, p. 10.

[81] Nedanovska et al. 2015.

2.7 *Plasma kernel dynamics*

So far, we have been mainly concerned with examining the evolution of toroidal plasmas generated by a single laser-induced breakdown plasma. We visualised and interpreted the responsible fluid flow, and throughout these discussions the highly symmetrical nature of the two-lobe breakdown plasma proved to be of some importance.

Experimental laser-induced breakdown studies,[82] just as numerical studies on the fluid dynamical effects of laser energy deposition,[83] likewise report similar toroidal structures, but instead observed highly asymmetrical tear-drop shaped breakdown plasmas.

More recent studies addressing the onset and dynamics of plasma

[82] Nassif et al. 2000; Harilal et al. 2015; Bak, Wermer et al. 2015; Dumitrache et al. 2017; Bradley et al. 2004; Bak, Im et al. 2014.

[83] Ghosh et al. 2008; Morsy et al. 2002.

kernels, however, do report plasmas with a two-lobe structure similar to those observed in our experiments.[84] Different mechanisms have been identified, including self-focussing, lens aberration, and hydrodynamic instabilities,[85] but the onset and dynamics of plasma kernels is still not very well understood.[86]

The lately reported kernels[87] even show a striking resemblance to the laser-induced breakdown plasmas observed in our experiments. To relate these observations to each other, this section presents high temporal resolution images of our breakdown plasma, compares them to the lately reported plasma kernels, and correlates photo detector measurements of the laser pulse intensity with intensity measurements obtained through integration of the recorded images.

[84] Nishihara et al. 2018; Alberti, Munafò, Pantano et al. 2019a.

[85] See Nishihara et al. 2018 and references therein.

[86] Alberti, Munafò, Pantano et al. 2019b.

[87] Alberti, Munafò, Koll et al. 2020; Alberti, Munafò, Pantano et al. 2019b.

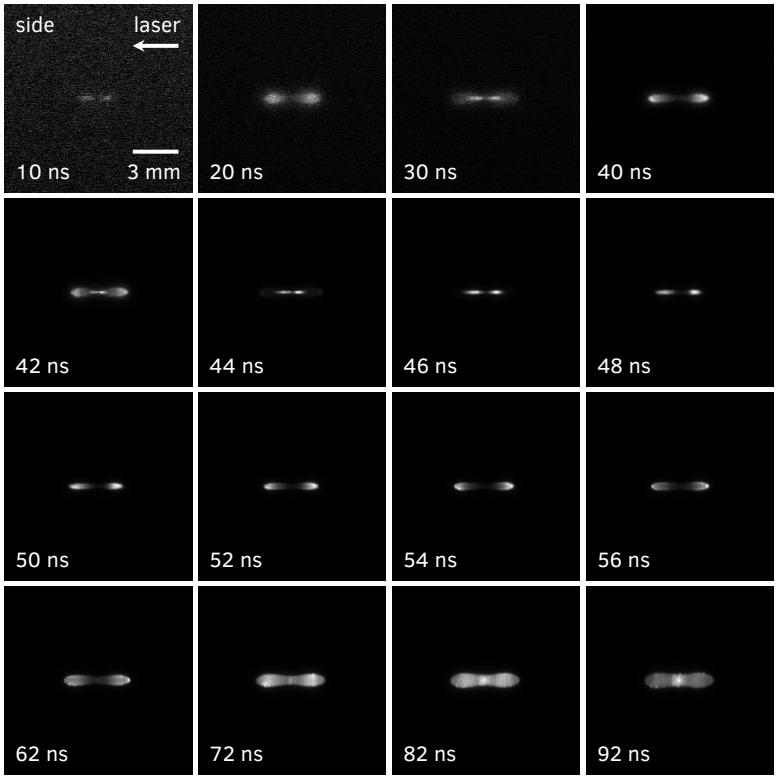

Figure 2.26: Early development of a laser-induced breakdown plasma showing the repeating dynamics of the two-lobe structure in the plasma kernel. The high temporal resolution side view images have been captured at increasing times after the laser trigger. Note that $t = 0$ has no physical meaning and is arbitrarily chosen. (10–20 ns) Small and faint expanding two-lobe plasma. (30–40 ns) Another smaller but brighter expanding two-lobe plasma. (42–92 ns) Another, even smaller and brighter, expanding two-lobe plasma which will develop into the principal breakdown plasma (see text for details). The images have been individually normalised to their maximum intensity. Laser pulse energy: 275 mJ, focal length focussing lens: 50 mm, helium gas pressure: 1000 mbar, bandpass filter: none, ICCD camera gate width: 2 ns, ICCD camera image averaging: none.

In figure 2.26 we present a selection of images recorded with an exposure time of 2 ns while using a laser pulse energy of 275 mJ. The images have been captured at increasing times after the laser trigger and without using a bandpass filter. Note that $t = 0$ bears no physical meaning and is arbitrarily chosen.

The integrated intensity of the recorded images is presented in figure 2.27, together with separately obtained intensity measurements using a photo detector. Synchronisation of the integrated intensity with the measurements obtained using the photo detector has been done by correlating their intensity curves and translating the photo detector measurements in the time domain until they overlap.

The intensity measurements show a 4 ns delay between the emission of the principal breakdown plasma and the laser pulse, before it relaxes exponentially over greater time scales. Remarkably, tens of nanoseconds before the main laser pulse is observed, a faint plasma is visible in the recorded images. We attribute this to the formation of the giant pulse in our Q-switched Nd:YAG laser. Initially the photon density starts at a

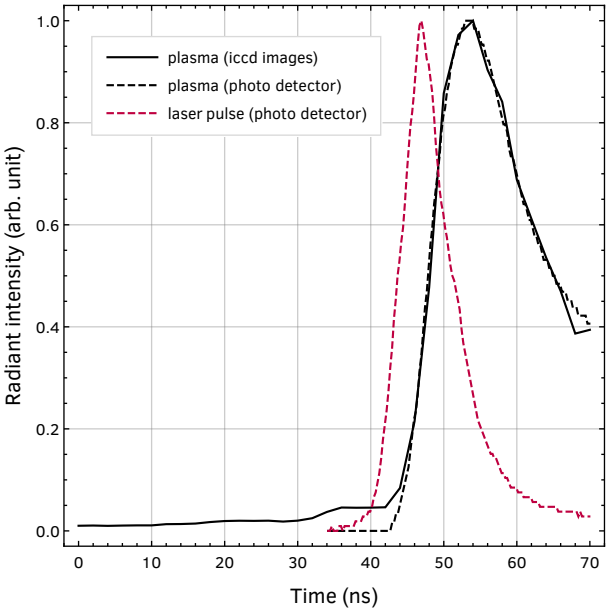

Figure 2.27: Radiant intensity of the plasma kernel (dashed black line) and laser pulse (dashed purple line) recorded through a photo detector, overlaid with the integrated intensity of the plasma kernel images presented in figure 2.26 (solid black line). Note the 4 ns delay between the laser pulse and the emission of the principal breakdown plasma. The intensity traces have been individually normalised to their maximum intensity and averaged over 100 recordings. The temporal axis represents time after the laser trigger. Note that $t = 0$ has no physical meaning and is arbitrarily chosen, but identical to the plasma kernel images presented in figure 2.26.

low value, and then grows at an approximately exponential rate before forming the giant pulse.[88] During the exponential growth, the photon density is small compared to the giant pulse, but it can nevertheless be sufficient to induce breakdown and create a faint plasma. The photo detector does not observe this weak emission, most probably due to a minor misalignment or an incorrect bias setting of the detector.

[88] Wagner et al. 1963.

In the images presented in figure 2.26, a small and faint two-lobe plasma is discernible some 30 ns before the advent of the main laser pulse. This two-lobe plasma slightly expands for 20 ns, after which a second, smaller but brighter, two-lobe plasma is observed, within the already present plasma. This plasma likewise expands for 12 ns, after which, once again, an even smaller but still brighter, two-lobe plasma is observed at 42 ns, marking the beginning of the main laser pulse. At the end of the laser pulse, the two-lobe plasma fills up and emission is observed from the entire elongated plasma. This is clearly visible in the recorded images from 72 ns onward.

In general a laser-induced breakdown plasma is created as a result of avalanche ionisation, where multi-photon ionisation provides the initial seed electrons necessary to ignite the avalanche.[89] Subsequent inverse bremsstrahlung absorption heats the plasma[90] creating a high pressure and high temperature plasma kernel whose rapid expansion leads to the formation of a shock.[91] The repeating dynamics observed in our plasma kernel possibly contributes to the formation of the two-lobe structure by successively creating small low density cavities, thereby increasing the breakdown threshold and inhibiting the creation of additional plasma in the central region.

[89] Raizer 1991, p. 155.

[90] Miziolek et al. 2006, p. 171.

[91] Alberti, Munafò, Pantano et al. 2019a; Y. Chen et al. 2000; Harilal et al. 2015; Ghosh et al. 2008.

The plasma kernels presented in this work strikingly resemble the images reproduced in figure 2.28, which have recently been reported in studies on the onset and dynamics of plasma kernels.[92] The non-equilibrium three-temperature plasma model presented therein is in good agreement with experimental observations and accounts for multi-

[92] Alberti, Munafò, Koll et al. 2020; Alberti, Munafò, Pantano et al. 2019b; Alberti, Munafò, Pantano et al. 2019a.

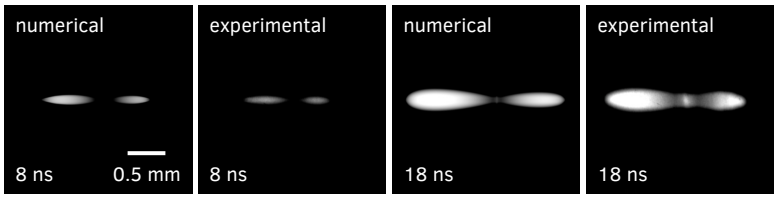

Figure 2.28: Laser-induced breakdown plasmas created in quiescent atmospheric pressure air. The two-lobe plasma kernels strikingly resemble the kernels presented in figure 2.26. These images are reproduced from a numerical and experimental study on plasma kernel dynamics (Alberti, Munafò, Koll et al. 2020) with permission of the Institute of Physics Publishing.

photon ionisation, inverse bremsstrahlung absorption, chemical kinetics, shock dynamics, and radiation propagation. Despite addressing laser-induced breakdown in air, which necessitates a chemical kinetics component accounting for the plasma chemistry of the constituents of air, their model is still in good agreement with our observations.

2.8 Conclusion

In this chapter, we have examined self-organising toroidal plasmas, generated solely by a single laser-induced breakdown plasma, created in quiescent atmospheric pressure helium gas at room temperature. We addressed many aspects of its development and found the generation to be robust over a wide range of laser pulse energies.

We tomographically reconstructed the poloidal radiant intensity profile of a toroidal plasma for its entire evolution, using a novel numerical method based on transform techniques for the Abel inversion. We used this reconstruction to visualise the fluid flow responsible for the development of the toroidal structure, and presented a first observation of the eroding and splitting of the toroidal plasma caused by the symmetrical nature of the two-lobe plasma kernel.

The origin of this flow is found to stem from the fluid flow repleting the low density cavity, created in the wake of a shock generated by the laser-induced breakdown plasma. In support of the existence of this cavity, we measured the evolution of the density of helium atoms in the centre of the toroidal plasma, with the use of a second laser-induced breakdown plasma.

We established a characteristic time scale at which structure is expected to develop. For a laser-induced breakdown plasma, created in quiescent atmospheric pressure helium gas at room temperature using a laser pulse energy of 250 mJ, the characteristic time scale is found to be approximately 16 µs, in agreement with our calculated value of 13.4 µs.

We found that the symmetrical nature of the toroidal plasma stems from the symmetrical fluid flow repleting the low density cavity, which is supported by flow experiments where the symmetrical experimental setting is deliberately broken by placement of a metal sheet close to the laser focus. By breaking the symmetry, vorticity has been introduced in the toroidal plasma.

We presented nanosecond temporal resolution recordings of the evolution of the plasma kernel, and observed a novel repeated creation of plasma that we attribute to the formation of the giant pulse in the Q-switched Nd:YAG laser. This repeating dynamics contributes to the

formation of the two-lobe structure of the plasma kernel.

The observed laser-generated transient toroidal helium plasmas are robust toroidal structures created under atmospheric pressure ambient conditions. These properties indicate that they provide an interesting setting for investigating the self-organising knotted magnetic structures in plasma introduced at the outset of this chapter.

To strengthen our understanding of the development of the toroidal plasmas, our next steps will include measurements that further support the existence of the aforementioned low density cavity, and measurements that characterise the plasma parameters of the toroidal plasmas, like the electron number density and the electron collision rate. These experiments will be presented in chapters 3 and 4 of this dissertation.